Diagnosis of the Imploding Shell Asymmetry in Polar-Direct-Drive Deuterium–Tritium Cryogenic Target Implosions on OMEGA

T. R. Joshi, R. C. Shah, W. Theobald, K. Churnetski, P. B. Radha, D. Cao, C. A. Thomas, J. Baltazar, and S. P. Regan

Laboratory for Laser Energetics, University of Rochester

The polar-direct-drive (PDD)[1–6] approach has been developed for performing laser-direct-drive inertial confinement fusion (ICF) experiments at the National Ignition Facility (NIF)[7] using the current configuration of laser beams customized for indirect-drive implosions. The NIF lacks beams near the equator for a symmetric illumination; therefore, the beams must be repointed to adequately irradiate the equator for direct-drive experiments.[8,9] The repointed beams have decreased energy coupling with the target, thereby requiring higher drive energies and unique pulse shapes to prevent reduced drive uniformity.[4] The irradiation nonuniformity caused by the PDD geometry reduces the implosion performance of OMEGA[10] ambient target implosions,[3,6] but it has never been evaluated in cryogenic target implosions. There is an ongoing effort on OMEGA to understand the hydrodynamic scaling of the best-performing symmetrically irradiated cryogenic target implosions,[11] as well as to study the impact of a PDD illumination geometry in order to improve our understanding of scaling from OMEGA to future NIF direct-drive cryogenic target implosions. The 40-beam PDD configuration on OMEGA provides a good approximation to the NIF PDD conditions.[1] However, differences remain in terms of the beams' angle of incidence, number of beams, number of rings, flexibility in laser pulse shaping, and laser smoothing.[4]

X-ray[2–4] radiography and self-emission imaging[12–14] techniques have been widely used to measure shell asymmetries and trajectories of imploded shells on OMEGA and the NIF. In this summary, we have extended the application of the x-ray self-emission imaging technique to PDD ICF implosions with cryogenically layered deuterium–tritium (DT) targets on OMEGA. The in-flight shell asymmetries were diagnosed at various times during the implosion, which were caused by the beam-pointing geometry and pre-imposed variations in the energy partition between the different groups of laser beams.

PDD ICF experiments with cryogenically layered DT targets were performed for the first time on OMEGA. The PDD illumination was achieved by using 40 of the 60 OMEGA[10] UV beams by switching off 20 beams around the equator. Figure 1(a) shows a schematic map of the OMEGA target chamber with the blue circles indicating the used beam ports. The 40 beams are grouped in three beam rings in the upper and lower hemisphere according to their polar angles. The beams were repointed to achieve the best possible illumination uniformity.[6] In each group of six rings, there were five, five, and ten laser beams, respectively. Figure 1(b) shows the beam pointing scheme, which was fixed during the experiment. The dashed lines indicate the repointing locations for the beams from the upper hemisphere. The beams from rings 1, 2, and 3 were repointed by 123 μm, 157 μm, and 219 μm, respectively. The displacement represents the distance from the target center along the direction perpendicular to the beam axis. The pointing condition was optimized with pre-shot *DRACO*[15] simulations.

All targets contained a DT ice shell overcoated by a thin plastic (CD) ablator layer, and the core of the shell was filled with DT vapor. The outer diameter of the CD shell was 767 μm and the thicknesses of the CD ablator and the DT ice layer were 6.2 μm and 33.5 μm, respectively. The laser pulse consisted of a picket that launched a shock controlling the shell adiabat ($\alpha \approx 4$, ratio of plasma pressure to the Thomas–Fermi pressure at peak density) and then gradually rose to a 1.4-ns dual-step main drive pulse [see Fig. 1(c)]. The total UV laser energy on target was 12.7$\pm$0.2 kJ, where the average was calculated for a set of five shots (three shots are discussed here) and the error represents the standard deviation. All 40 beams were outfitted with small-spot distributed phase plates (SG5-650),[16–18] polarization smoothing,[19] and 2-D smoothing by spectral dispersion[20] at 0.3-THz bandwidth and

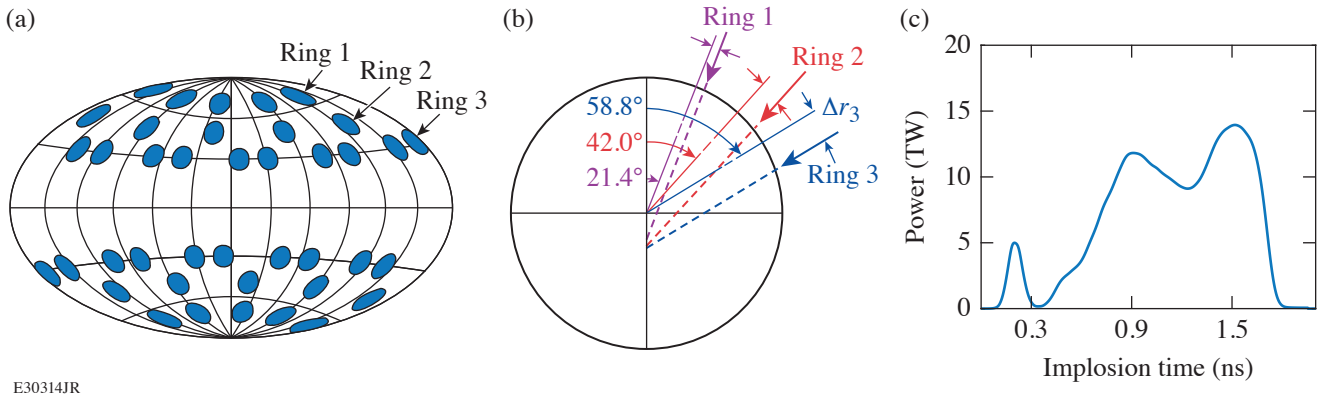

Figure 1
(a) Beam-port configuration for a PDD implosion on OMEGA. (b) Beam-pointing schemes and target geometry. The dashed lines show the shifted beams for OMEGA PDD geometry. (c) Pulse shape used for the implosions.

three-color cycles.[21,22] The partition of beam energies in rings 1 and 3 was varied while keeping the total laser energy constant. By denoting with ΔE_3 the change in energy of ring 3 (irradiating closer to the equator) and with ΔE_1 the change in energy of ring 1 (irradiating closer to the pole), the change in ring energy ratio is defined as $\Delta D = (\Delta E_3 - \Delta E_1)/E_{\text{tot}}$, where E_{tot} is the total energy on target. The nominal ring energy partition for a balanced drive ($\Delta D = 0$) is $E_1/E_{\text{tot}} = 0.25$, $E_2/E_{\text{tot}} = 0.25$, and $E_3 E_{\text{tot}} = 0.5$. Table I shows a summary of the discussed shots with drive imbalance condition, parameter ΔD, total laser energy on target, energy in each ring, and the measured neutron yield.

Table I: Summary of the shot number, drive imbalance condition, drive imbalance parameter, total laser energy on target, energy in each ring, and the measured neutron yield from DT fusion reactions.

Shot number	Drive	ΔD	E_{tot}(kJ)	E_1 (J)	E_2 (J)	E_3 (J)	Neutron yield (10^{13})
96575	Balanced	1.0%	12.7	3132	3155	6433	1.32±0.09
96578	Strong on poles	−4.6%	12.9	3522	3203	6173	1.93±0.07
96581	Stronger on equator	−10.6%	12.9	2560	3190	7158	1.34±0.09

The x-ray emission from the shell was recorded temporally and spatially resolved during the acceleration phase of the implosion with two pinhole cameras coupled to x-ray framing cameras in TIM-1 ($\theta = 63.44°$, $\varphi = 126°$ and in TIM-5 ($\theta = 101.81°$, $\varphi = 270°$), where TIM stands for ten-inch manipulator and θ and φ, respectively, are the polar angle and azimuthal angle coordinates of the OMEGA target chamber ports. An array of sixteen 15-μm-diam pinholes were used to produce 16 temporally resolved x-ray self-emission images[12,13,23] of the target on a four-strip x-ray framing camera.[24,25] Figure 2 shows x-ray self-emission images from the TIM-1 camera after the laser burned through the outer CD layer. The outer and inner rings in the images come from the emission at the CD–DT interface and the DT ice layer ablation front, respectively.[13] Here only the DT ablation front is analyzed because of its close proximity to the dense DT shell. The emission from the outer CD–DT interface layer is quickly diminishing in time due to the evaporation and rarefaction of the material in the plasma corona. Images in Figs. 2(a)–2(c) were acquired from shots 96578, 96575, and 96581, respectively, and at roughly the similar times relative to the start of their laser pulses. In shot 96578, the target is driven stronger on the poles with $\Delta D = -4.6\%$ and the shape of the DT ablation front in the measured image in Fig. 2(a) is oblate. In shot 96581, the target is driven stronger on the equator with $\Delta D = 10.6\%$ and the shape of the DT ablation front becomes prolate as shown in Fig. 2(c). In shot 96575, the drive was more balanced, and consequently a rounder shape can be seen in Fig. 2(b). Similar images were obtained from the TIM-5 camera. The shape of the DT ablation front was determined by tracking the peak x-ray emission in the inner ring with respect to the polar angle in the image plane.

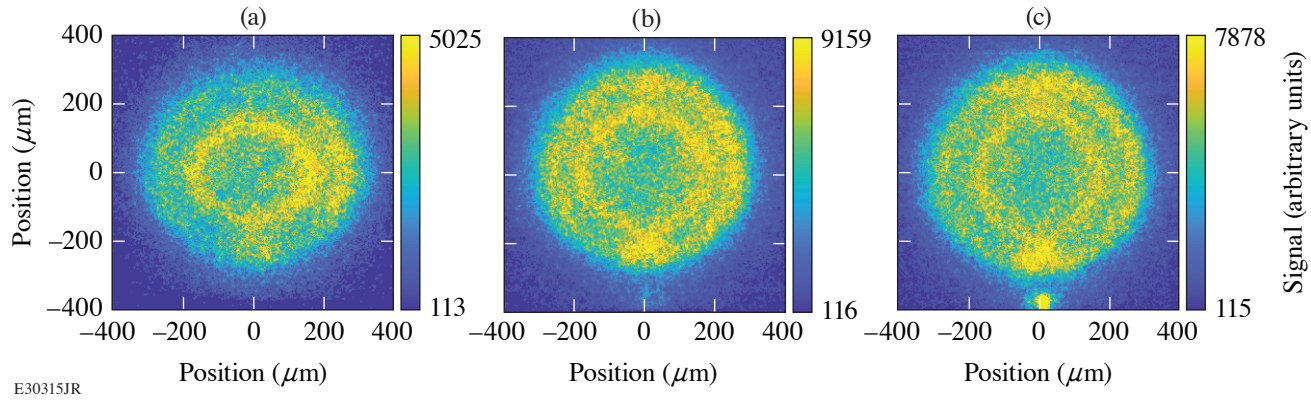

Figure 2
Measured x-ray self-emission images from three shots with different laser drive balance. Images from shots (a) 96578 (ΔD = −4.6%), (b) 96575 (ΔD = 1.0%), and (c) 96581 (ΔD = 10.6%). The camera was positioned in TIM-1 (θ = 63.44°, φ = 126°). The x-ray self-emission images in (a)–(c) were recorded at 1.67±0.1 ns, 1.62±0.1 ns, and 1.58±0.1 ns, respectively, relative to the start of the laser pulse in their implosions.

Figure 3 shows the temporal evolution of P_2 from the three shots with different drive imbalance from the two different lines of sight (TIM-1 and TIM-5). The normalized mode amplitude is plotted along the ordinate versus the ablation-front radius on the abscissa. Since the ablation-front radius decreased with time during the compression phase, the corresponding time axis progresses from right to left. The P_2 amplitude magnitude at a large radius of ~350 μm (early time) is similarly small (<2%) for all the shots. The P_2 amplitude of the targets before the shots was measured to be <0.3% (Ref. 26). Both views show similar trends, although there are slight differences in the P_2 amplitude, which might indicate a systematic error in the data analysis. The temporal evolution of modes 4 and 6 from the three shots with different drive imbalance remain similar within the measurement uncertainty, and modes higher than 6 are negligible. The sign of the P_2 amplitude indicates whether the shell is oblate (negative) or prolate (positive).[3,14] In Fig. 3, the P_2 amplitude of two different shots (96578 and 96581) have opposite signs, particularly in the later phase of the implosions. The P_2 amplitudes in shot 96575 are close to zero (slightly negative) and always lie in between the amplitudes from shots 96578 and 96581. Errors for each mode are estimated by the difference in extracted mode amplitude when fitting to the left and right halves of the ablation surface in the self-emission images separately. We recall here that the energy of each beam in ring 1 (close to pole) in shot 96578 was increased (ΔD = −4.6%) and that the energy of each beam in ring 3 (close to equator) in shot 96581 was increased (ΔD = 10.6%).

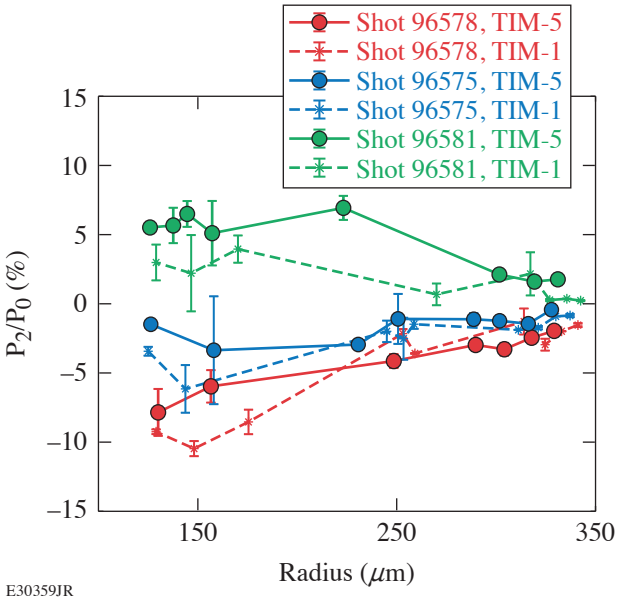

Figure 3
Comparisons of the temporal evolution of ℓ-mode 2 inferred from the shots 96578, 96575, and 96581 from the TIM-1 camera (star symbols, dashed lines) and the TIM-5 camera (circle symbols, solid lines).

Figure 4 shows that the extremum P_2 amplitude inferred from the TIM-1 and TIM-5 cameras varies linearly with the drive imbalance parameter ΔD. The dashed line represents a linear fit through all the data points. The slight vertical offset between the TIM-1 and the TIM-5 data set might indicate a systematic error in the data analysis. The P_2 amplitude is minimized for $\Delta D \sim 5\%$ and not as expected for $\Delta D = 0$. This might indicate that the energy coupling of non-normal laser rays in the equatorial region is over predicted in the current models. This trend also correlates with a 30% reduction in neutron yield (see Table I) for the shot with the largest ℓ-mode 2 amplitude. Future experiments will test the hypothesis of a minimal P_2 amplitude for a drive imbalance parameter of $\Delta D \sim 5\%$ for the current design and will perform similar experiments for designs with different shell adiabats. The observations of higher P_2 amplitudes in shot 96578 suggest that the shell asymmetry is higher when we increase the energies of the beams closer to the poles compared to the increase of the energies of the beams closer to the equator. This work will help to improve the understanding of the degradation mechanisms from the PDD beam geometry.

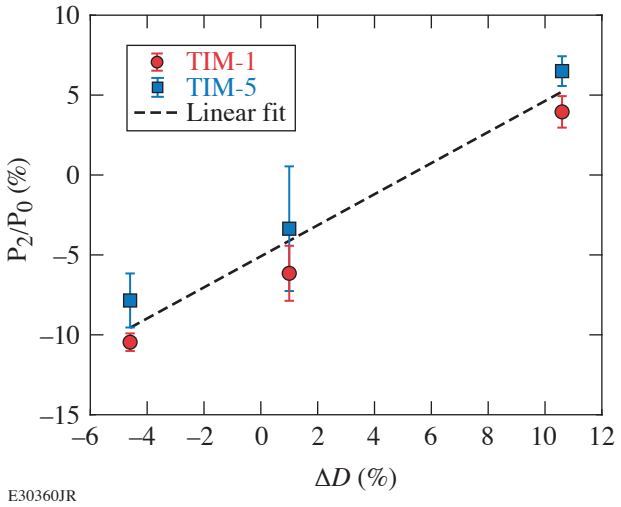

Figure 4
Inferred extremum P_2 amplitude versus drive imbalance parameter ΔD.

This material is based upon work supported by the Department of Energy National Nuclear Security Administration under Award Number DE-NA0003856, the University of Rochester, and the New York State Energy Research and Development Authority.

1. S. Skupsky *et al.*, Phys. Plasmas **11**, 2763 (2004).
2. R. S. Craxton *et al.*, Phys. Plasmas **12**, 056304 (2005).
3. F. Marshall *et al.*, J. Phys. IV France **133**, 153 (2006).
4. J. A. Marozas *et al.*, Phys. Plasmas **13**, 056311 (2006).
5. T. J. B. Collins *et al.*, Phys. Plasmas **19**, 056308 (2012).
6. P. B. Radha *et al.*, Phys. Plasmas **19**, 082704 (2012).
7. E. I. Moses, IEEE Trans. Plasma Sci. **38**, 684 (2010).
8. M. Hohenberger *et al.*, Phys. Plasmas **22**, 056308 (2015).
9. P. B. Radha *et al.*, Phys. Plasmas **23**, 056305 (2016).
10. T. R. Boehly *et al.*, Opt. Commun. **133**, 495 (1997).
11. V. Gopalaswamy *et al.*, Nature **565**, 581 (2019).
12. D. T. Michel *et al.*, Rev. Sci. Instrum. **83**, 10E530 (2012).
13. D. T. Michel *et al.*, Phys. Rev. Lett. **114**, 155002 (2015).
14. Y. Dong *et al.*, Plasma Sci. Technol. **22**, 084003 (2020).
15. P. B. Radha *et al.*, Phys. Plasmas **12**, 032702 (2005).
16. Y. Kato *et al.*, Phys. Rev. Lett. **53**, 1057 (1984).
17. T. J. Kessler *et al.*, Proc. SPIE **1870**, 95 (1993).
18. W. Theobald *et al.*, Phys. Plasmas **29**, 012705 (2022).

19. J. E. Rothenberg, J. Appl. Phys. **87**, 3654 (2000).
20. S. Skupsky *et al*., J. Appl. Phys. **66**, 3456 (1989).
21. *LLE Review Quarterly Report* **80**, 197 (1999).
22. S. P. Regan *et al*., J. Opt. Soc. Am. B **22**, 998 (2005).
23. A. K. Davis *et al*., Rev. Sci. Instrum. **87**, 11E340 (2016).
24. D. K. Bradley *et al*., Rev. Sci. Instrum. **63**, 4813 (1992).
25. D. K. Bradley *et al*., Rev. Sci. Instrum. **72**, 694 (2001).
26. D. H. Edgell *et al*., Fusion Science and Technology **49**, 616 (2006).